# Mechanical Design Considerations of a Light-Weight Rotor for Brushless Double Fed Machines


Malihe Heidary
*School of Engineering*
*University of East Anglia*
Norwich, UK
M.Heidary@uea.ac.uk

Salman Abdi, Senior Member, IEEE
*School of Engineering*
*University of East Anglia*
Norwich, UK
S.Abdi-Jalebi@uea.ac.uk

Hamidreza Mosaddegh-Hesar
*dept. of Electrical and Computer Engineering*
*University of Saskatchewan*
Saskatoon, SK, Canada
pvt356@mail.usask.ca

Xiaodong Liang, Senior Member, IEEE
*dept. of Electrical and Computer Engineering*
*University of Saskatchewan*
Saskatoon, SK, Canada
xil659@mail.usask.ca

Ehsan Abdi, Senior Member, IEEE
*Wind Technologies Ltd*
Cambridge, UK
Ehsan.Abdi@windtechnologies.com

Richard McMahon
*Warwick Manufacturing Group (WMG)*
*University of Warwick*
Coventry, UK
R.McMahon.1@warwick.ac.uk



***Abstract*—This paper presents an optimised rotor mechanical design to reduce the rotor mass of a Brushless doubly fed machine (BDFM). The rotor back iron is considered the area where iron materials can be removed from specific locations without compromising the rotor magnetic performance. The mechanical stress and vibration analyses are performed by Finite Element (FE) method using Ansys software to assess the practicality of the proposed design. This study is carried out on a prototype D400 250-kW BDFM, showing that the rotor mass can be reduced by about 4% with acceptable electromagnetic and mechanical operations of the machine in its rated operating conditions.**



***Index Terms*—Brushless doubly fed machine (BDFM), Finite-Element Method (FE), Mechanical stress, Modal analysis, Vibration, Rotor mass.**


## I. Introduction

Brushless doubly fed machines are attractive induction typed electrical machines with commercial promise to be used as both variable speed motors, and generators [1]. As a generator it is particularly attractive for wind power generation, and a promising replacement for doubly fed induction generators (DFIG) thanks to its brushless operation. Hence, BDFM has greater reliability, as well as, a medium speed range compared to high speed DFIG, leading to a significant simplification in the gearbox system [2]. A drivetrain based on BDFM technology is therefore believed to be simpler, more reliable and more cost effective compared to its DFIG counterpart. Medium speeds generators are becoming more popular for offshore wind generation as opposed to the direct-drive solutions where the low-speed generator and its fully-rated power converters are massively large and expensive. BDFM is therefore a viable solution to revolutionise the offshore wind market as a replacement to permanent magnet generators with fully rated converters requirements, since it only needs a fractional size converter in the range of 30-40% of the generator power ratings, and a simple one or two-stage gearbox system [3].

The BDFM has been explored for other applications, including as a stand-alone generator for off-grid applications [4], a variable speed drive [1], a synchronous compensator and flywheel energy storage system [5], marine propulsion [6], direct drive heavy-duty traction [7] and aviation turbo-electric propulsion [8]. There have been several attempts for constructing prototype BDFMs from small laboratory sizes up to several hundreds of kilowatts including a 250 kW size built by the authors [9], an 800 kW machine built for hydropower generation by Chen et al. [10], and most recently, a 120 kW high speed machine for aviation electric propulsion [11].

The BDFM stator design includes two sets of three-phase windings wound on a common stator core. The special rotor of a BDFM is designed to facilitate indirect coupling between the stator windings. A widely used rotor type is the nested loop rotor winding, although other rotor types have been reported to have acceptable performance [12–14].

To date, various research endeavors have focused on refining and optimising the design of this machine to achieve weight reduction [15–19]. Generally, BDFMs have higher power density and specific power compared to their counterparts. Consequently, a primary objective in optimising these machines' design is to minimise their mass and volume, a key emphasis of [15] proposing a lightweight and smaller BDFM in a given power output by reducing the stator back iron depth and removing iron materials from certain locations of the rotor back iron.

Both analytical method and Finite Element (FE) simulations confirmed that the proposed iron reductions do not affect the machine's magnetic circuit considerably at rated operating conditions. However, the proposed design has been solely founded on the electromagnetic operation of the BDFM, and

TABLE I
SPECIFICATIONS OF D400 BDFM

| **Motor Dimensions** | |
|---|---|
| Parameter | Value |
| Frame size | 400 |
| Air gap length | 439 $(mm)$ |
| Back iron depth | 54 $(mm)$ |
| Median diameter of stator back iron | 636 $(mm)$ |
| Stack length | 190 $(mm)$ |
| **Electrical parameters** | |
| Parameter | Value |
| PW pole pair | 2 |
| CW pole pair | 4 |
| PW rated voltage | 690 $(V)$ at 50 $(Hz)$ |
| CW rated voltage | 620 $(V)$ at 18 $(Hz)$ |
| PW rated current (line) | 178 $(A)$ |
| CW rated current (line) | 73 $(A)$ |
| Rated power | 250(kW) at 680 $(rpm)$ |
| Rated Torque | 3400 (N.m) |
| Speed range | 500 $(rpm) \pm 36$ % |

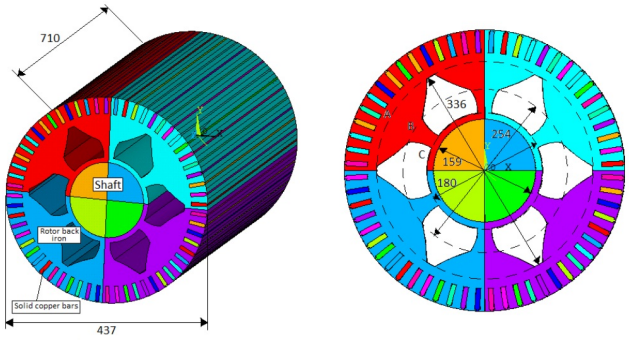


Fig. 1. 2D and 3D geometric geometry of D400 BDFM

TABLE II
BACK IRON MATERIAL PROPERTIES

| Material Name | VACOFLUX 48 |
|---|---|
| Yield Stress($\sigma_y$) | 190 $(MPa)$ |
| modulus of elasticity $(E)$ | 200 $(GPa)$ |
| Mass Density $(\rho)$ | 7700 $(Kg/m^3)$ |
| Poisson's ratio $(\vartheta)$ | 0.3 |

no study to assess the mechanical viability of the rotor design has been reported in [15]. This paper aims to bridge this gap by examining the feasibility of the proposed design from a mechanical perspective including stress analysis, displacement, modal analysis and natural frequencies. Additionally, it investigates the potential for further reduction in rotor mass beyond what the proposed design suggests in [15]. Optimising the rotor mass reduces material usage and rotational inertia, thereby lowering manufacturing costs and increasing efficiency, respectively. Also, using light-weight BDFM in wind turbine application can lead to a reduction in excessive force on the turbine tower and higher reliability by decreasing fatigue effect.

## II. MECHANICAL CONSIDERATIONS OF THE PROPOSED ROTOR DESIGN

The specifications of the prototype D400 BDFM is shown in Table I. The 2D and 3D models of the rotor are created by macro writing in Ansys software and illustrated in Fig. 1. The magnetic circuit analysis performed by the authors reported in [15] has shown that the two regions inside the dashed circle, A and B, do not take part in the magnetic circuit, and hence can be removed from the rotor core as far as the magnetic operation of the machine is concerned.

This paper therefore aims to propose an optimised rotor design by maximising the iron removal from the rotor back iron while having acceptable and reliable operation in terms of mechanical stress and vibration in a wide range of the machine operation. The BDFM rotor comprises a shaft, back iron, and copper bars. However, for this study, only the mechanical properties of the back iron are essential, as indicated in Table II.

### A. Stress Analysis

The type of stress experienced by the rotor in a BDFM is torsional stress, which occurs when the rotor is subjected to torque or twisting forces. The relationship between torsional stress in a solid shaft can be derived according to the theory of elasticity [20] as calculated in (1), where $T$ is applied torque, $c$ is shaft radius and $J$ is polar moment of inertia.

$$\tau_{max} = \frac{Tc}{J} \quad \text{(for solid circle} \quad J = \frac{\pi c^4}{2}) \tag{1}$$

Angular deflection is calculated by:

$$\phi = \frac{TL}{GJ} \tag{2}$$

where $L$ is length of shaft and for isotropic and homogeneous materials G (shear module) is:

$$G = \frac{E}{2(1+v)} \tag{3}$$

In (3), $E$ is Youngs modulus and $v$ is Poisson's ratio. The maximum torsional stress occurs on the outer surface of the shaft that is shown in Fig. 3. The rotor back iron includes 6 holes based on the proposed design in [15], leading the value of the polar moment of inertia decreases compared to a solid circular rotor.

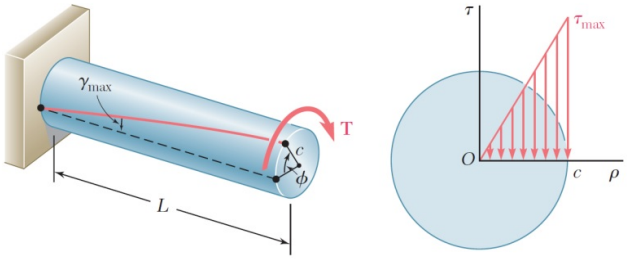


Fig. 2. Torsional stress and deflection

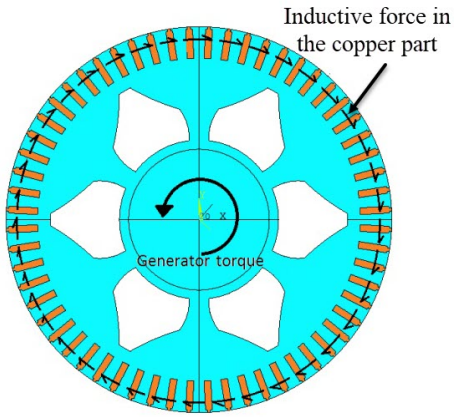


Fig. 3. The studied rotor

The stress analysis on the rotor is conducted using Ansys software by both 2D and 3D models in this study. It should be mentioned that the shaft is assumed fixed to enable a static analysis, however, the stress values are subsequently adjusted to reflect dynamic conditions by applying appropriate coefficients.

*1) 2D Analysis:* The simulated 2D model in X-Y plane is shown in Fig. 3. To conduct the stress analysis, the rated torque of 3400 N.m is applied to the region beyond the dashed line circle A in the rotor in Fig. 1. The torque is mainly applied to the area of the copper parts and its surroundings. Also, static conditions have been applied on the shaft and all nodes related to the shaft are fixed in both X and Y directions since the analysis is conducted statically as shown in Fig. 4. The torque distribution involves allocating 3400 $N.m$ among various nodes, with each node representing a specific copper component. The force on each node can be calculated as:

$$\begin{cases} T = nT_n = n(F_n \times d_n) = n(F_n.d_n.cos(90)) = nF_nd_{ave} \\ F_n = \frac{T_t}{nd_{ave}} \end{cases} \tag{4}$$

where, $T_t$, $n$, $F_n$, $d_n$, and $d_{ave}$ are total torque, number of nodes, force value on each node, distance value from center for each node and average distance of nodes from center, respectively. Applying a load to the machine allows calculating the displacement in each node using FE analysis. Subsequently, stress values in various directions can be determined. However, a compound stress model is needed, which varies depending on the chosen design method. Von Mises compound stress is utilised in this study, and the contours depicting total displacement and Von Mises stress resulting from the 2D model are illustrated in Fig.6. As can be seen in Fig. 6(a), the maximum displacement is less than 1 m that indicates minimal impact on motor operation. Fig. 6(b) shows that the maximum Von Mises stress is 1.42 $MPa$, occurring at the thickest part of the rotor as anticipated by Saint-Venant's Principle and stress concentration. To validate the accuracy of the results performed by 2D model, the mesh independency study should be performed.

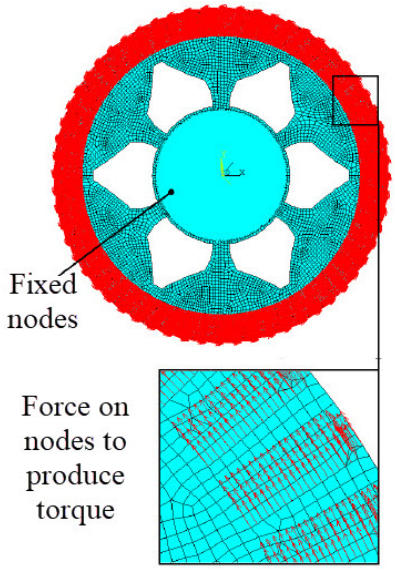


Fig. 4. Boundary conditions on 2D model

One of the suitable criteria for this study involves assessment of the strain energy by incrementally increasing the number of elements. However, the calculation of the total strain energy cannot be used for 2D models, so the maximum deflection criterion is used to check the independency of the mesh that is shown in Fig. 5. It can be seen that the maximum deflection value does not change significantly after increasing the number of elements to 10,000, so the completed mesh can be considered independent of the number of elements.

*2) 3D Analysis:* 3D model of the BDFM rotor is considered as shown in Fig.1 to provide a more realistic model of the rotor. The obtained results for 3D model including contour of total displacement and Von Mises stress are shown in Fig. 7. The comparison between 2D and 3D models, as illustrated in Table III, shows close agreement between the results obtained from both models. Consequently, the subsequent analyses will be carried out using the 2D model to simplify the process. Validating the results of the 3D model through the strain energy method also indicates that increasing the number of elements to more than 60,000 results in negligible changes in the total strain energy. Furthermore, the generated mesh remains independent of the number of elements above 10,000 elements.

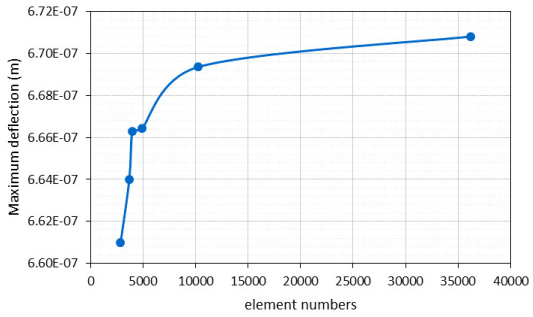


Fig. 5. Maximum value of displacement relative to the number of elements

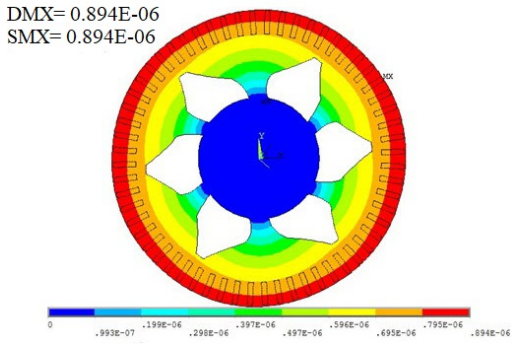


(a)

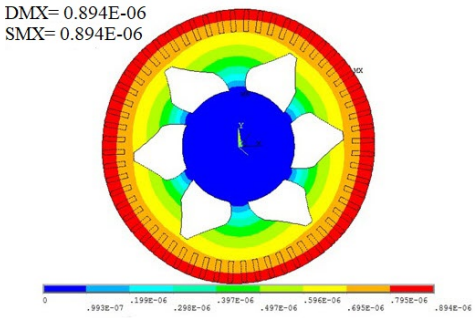


(b)

Fig. 6. Stress analysis results for 2D model (a)- Contour of total displacement (m) , (b)- Contour of Von Mises stress (Pa)

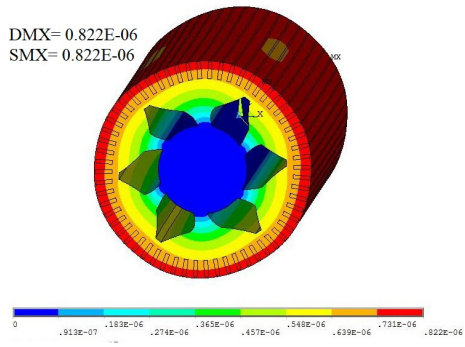


(a)

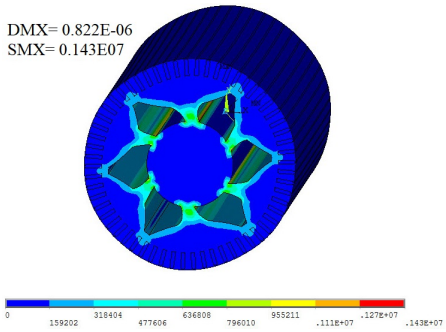


(b)

Fig. 7. Stress analysis results for 3D model (a)- Contour of total displacement (m), (b)- Contour of Von Mises stress (Pa)

TABLE III
COMPARISON BETWEEN 2D AND 3D RESULTS

| Model Type | Maximum deflection $(m)$ | Maximum Von Mises Stress $(Pa)$ |
|---|---|---|
| 2D | 0.894E-06 | 0.142E07 |
| 3D | 0.822E-06 | 0.143E07 |

TABLE IV
FREQUENCIES OBTAINED BY 2D AND 3D MODAL ANALYSES

| Mode type | Frequencies $(Hz)$ | 2D/3D modeling |
|---|---|---|
| Bending vibration | 1053.3 | 3D Vibration in X-Z plane |
| Bending vibration | 1062.4 | 3D Vibration in Y-Z plane |
| Torsional vibration | 1123.8 | 2D Vibration in X-Y plane |
| Axial vibration | 1710.3 | 3D Vibration in Z direction |

### *B. Vibration Analysis*

In general, the rotor of an electric motor can vibrate in different directions, which can be summarised as follows [20]:

- Lateral vibration: Defined as an oscillation that occurs in the radial plane of the rotor spin axis which causes dynamic bending of the shaft in two mutually perpendicular lateral planes.
- Torsional vibration: Defined as angular vibration that occurs about the axis of a shaft, which involves speed fluctuations of various components and the twisting of shaft sections while the machine is rotating.
- Axial vibration: Defined as an oscillation that occurs along the axis of the rotor which is associated with the extension and compression of the rotor along its axis.

Hence, a three-dimensional model of the rotor is needed to investigate the lateral and axial vibrations. The resulting frequency modes are oshown in Table IV, with the first and second modes representing bending vibrations in the XZ and YZ planes. Although the frequencies of these two modes are nearly identical, any slight discrepancy can be due to the mesh and time step considered in simulations. The subsequent vibration mode is the torsional mode, occurring at a slightly higher frequency. The fourth vibration mode pertains to axial vibrations, which occurs at significantly higher frequencies in comparison with the other modes. These natural frequencies can be compared with rotational frequencies, given that the motor operates at various RPMs.

Table I indicates that the highest rotor speed, denoted as the rated speed, is 680 $rpm$, converting this rotational speed to hertz yields 11.33 Hz, so the vibration behaviour of the system is expected to be stable as there is a considerable gap between the value of excitation frequency and natural frequencies. This can be confirmed by the Campbell's diagram that is used to check the effect of rotational speed changes on natural frequencies and identify critical speeds and potential resonance issues. In this diagram, the x-axis represents various operational speeds of the rotor, while the y-axis depicts the rotor's natural frequencies that vary along with the rotational speed [21].

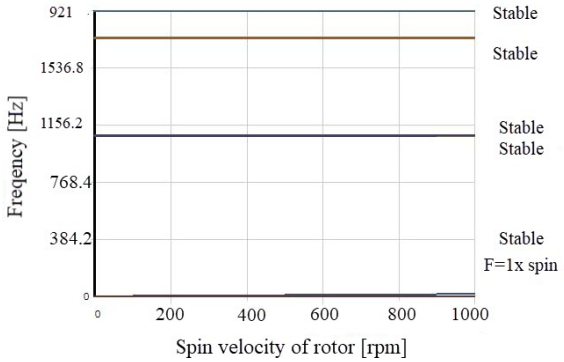


Fig. 8. Campbell diagram for 3D Rotor model

As can be seen in the plotted diagram for the 3D model shown in Fig. 8, the natural frequencies remain stable, maintaining their values regardless of the increasing excitation frequency. This consistency in natural frequencies owes itself to the solid geometry of the studied rotor. Therefore, analysing the vibration behavior of the rotor under study becomes straightforward through a comparison of its excitation frequency (rotor speed) with the natural frequencies.

## III. Rotor Optimisation

In this section, the rotor mass reduction is studied to achieve the maximum allowable iron reduction by considering the mechanical stresses discussed in Section II. In [15], it has been shown by magnetic analysis that it is not feasible to reduce the material of the rotor between the circles delineated by dashed lines A and B any further. Therefore, the main focus of this study is on reducing rotor mass between the circles labeled B and C. A parameter $P$ is defined as shown in Fig. 9 to alter the shape of the surface area removed from the rotor. Fig. 10 shows six different cases when $P$ varies from 1 ° to 6 °, resulting the area of the holes inside the rotor core to expand. Mass and area reduction for each case is presented in Table V.

### A. *Displacement and stress in static analysis*

In this section, the static stress analysis is carried out for each of the above six cases, and the 2D model is employed to reduce the volume of the numerical calculations. The maximum values of Van Mises stress and displacement are summarised in Table VI for all six cases of Fig. 10.

TABLE V
Area and Mass Reduction for Each Considered Model

| Angle ($P$) | Area($m^2$) | Total mass ($Kg$) | Reduction (%) |
|---|---|---|---|
| 0° | 0.11971 | 755.8489 | 0 |
| 1° | 0.11873 | 749.6612 | 0.8 |
| 2° | 0.11776 | 743.5366 | 1.6 |
| 3° | 0.11680 | 737.4752 | 2.4 |
| 4° | 0.11586 | 731.54 | 3.2 |
| 5° | 0.11494 | 725.7312 | 4 |
| 6° | 0.11403 | 719.9854 | 4.7 |

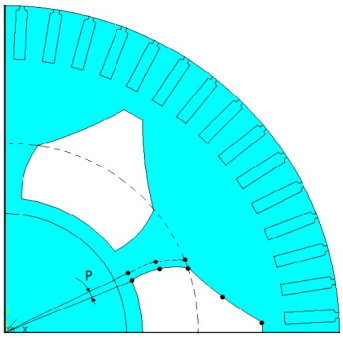


Fig. 9. Definition of angle $P$ for reducing rotor area

To assess the obtained stresses, the safety factor is calculated using (5), according to the IEC 61400-1 standard.

$$n.S_d \leq S_s \tag{5}$$

where, $n$, $S_d$, and $S_s$ are safety factor, obtained stress by FE model and material yield stress which is 190 $MPa$ for the studied rotor, respectively. Therefore safety factor for the studied models can be calculated by dividing Maximum Von Mises Stress by 190, which are shown in Table VII.

According to this Table, the obtained safety factor from $P$= 1 ° to $P = 5$ ° is significantly more than the standard safety value according to IEC 61400-1 ($n$=3.56), but at $P = 6$ ° the value of safety factor is slightly higher than the permissible limit. However, since the effects of thermal stress, fatigue and environmental conditions such as humidity are not considered in this study, $P = 5°$ is selected as the optimised design, meeting the required safety margin and reduces the rotor volume by about 4%.

### B. *Vibration analysis*

The vibration analysis is performed for the studied six cases, and the obtained frequencies along with those calculated for $P = 0$ ° in II-B are presented in Table VIII. In general, frequencies in close proximity to the rotational speed of a rotor are particularly susceptible to inducing vibration and escalating the risk of resonance.

TABLE VI
Maximum Von Mises and Displacements Values for Each Model

| Angle ($P$) | Maximum deflection ($m$) | Maximum Von Mises Stress ($Pa$) |
|---|---|---|
| 1° | 0.82E-06 | 1.73E06 |
| 2 ° | 1.07E-06 | 2.10E06 |
| 3 ° | 1.51E-06 | 2.80E06 |
| 4 ° | 2.48E-06 | 3.97E06 |
| 5° | 5.47E-06 | 8.12E06 |
| 6 ° | 5.47E-06 | 39.3E06 |

TABLE VII
Factor of Safety for the Studied Models

| Angle ($P$) | 1° | 2° | 3° | 4° | 5° | 6° |
|---|---|---|---|---|---|---|
| Safety factor | 109.8 | 90.47 | 67.8 | 47.8 | 23.4 | 4.83 |

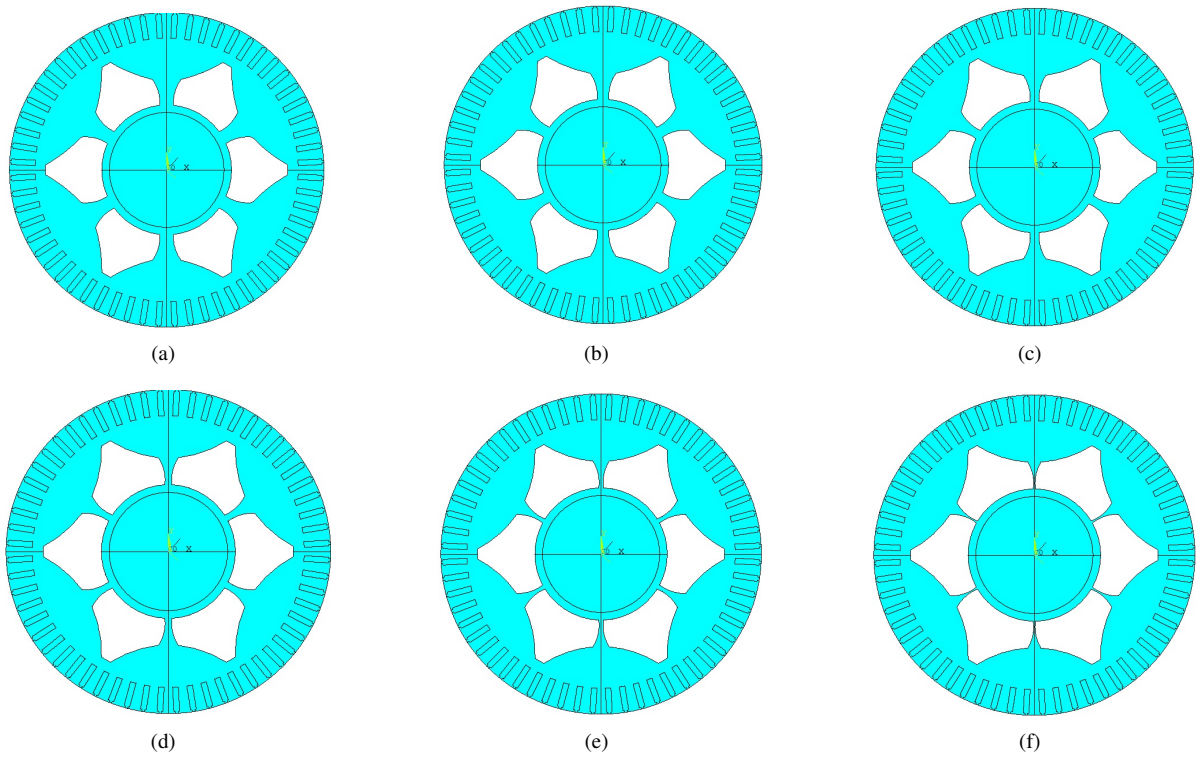

Fig. 10. Six considered models with different angles. (a)- $P = 1$ °, (b)- $P = 2$ °, (c)- $P = 3$°, (d)- $P = 4$ °, (e)- $P = 5$ °, (f)-$P = 6$ °

TABLE VIII
OBTAINED FREQUENCIES FOR EACH MODEL ($Hz$)

| Angle ($P$) | Bending mode in x-z plane | Bending mode in y-z plane | Torsional mode in x-y plane | Axial mode in z direction |
|---|---|---|---|---|
| 0° | 1053.3 | 1062.4 | 1123.8 | 1710.3 |
| 1 ° | 1038.7 | 1039.1 | 983.1 | 1656.1 |
| 2 ° | 1018.1 | 1018.2 | 860.1 | 1602.3 |
| 3 ° | 991.5 | 992.3 | 722.1 | 1536.9 |
| 4 ° | 952.1 | 956.5 | 562.3 | 1451.6 |
| 5 ° | 897.1 | 901.4 | 377.9 | 1322.7 |
| 6 ° | 799.1 | 803.9 | 157 | 1073.2 |

This phenomenon, termed 'rotational resonance,' occurs when external forces or disturbances align with or closely approach the natural frequency of a rotating system, such as the rotational speed of a rotor. Therefore, at $P = 0$ °, the dominant frequency is the bending frequency, given its proximity to 11.33 Hz.

However, as the value of P increases, the torsional frequency in the X-Y plane becomes dominant, approaching the rotational frequency. It is worthwhile to mention that the possibility of resonance is minimal and all the studied models are not at risk of vibration-related issues due to the existing large gap between the obtained frequencies and the rotational speed frequency.

## IV. CONCLUSION

In this paper, the rotor of D400 BDFM is studied in terms of mechanical strength and its rotor volume is optimised to have a light-weight motor. The performed analysis is done by written macro codes in Ansys software to be able to define considered holes inside the rotor core parametrically, then each model is analysed regarding stress and vibration considerations.

Modal vibration analysis is conducted to determine the natural frequencies at different angles, indicating that the frequency of rotor speed is notably lower than the obtained frequencies. Campbell's diagram related to the models is also extracted which shows that natural frequencies are independent of the rotor speed, so the vibration behaviour of all 6 models can be considered stable. Finally, according to the performed analyses model 5 with $p = 5$ ° is selected as the optimised model.

## REFERENCES


[1] S. Shao, E. Abdi, and R. McMahon, "Operation of brushless doubly-fed machine for drive applications," in *2008 4th IET Conference on Power Electronics, Machines and Drives*, pp. 340–344, IET, 2008.

[2] S. Abdi, S. Sharifzadeh, and S. Amiri, "Reliability model development for wind turbine drivetrain with brushless doubly-fed induction machine as generator," in *2021 22nd IEEE International Conference on Industrial Technology (ICIT)*, vol. 1, pp. 228–233, IEEE, 2021.

[3] G. van de Kaa, M. van Ek, L. M. Kamp, and J. Rezaei, "Wind turbine technology battles: Gearbox versus direct drive-opening up the black box of technology characteristics," *Technological Forecasting and Social Change*, vol. 153, p. 119933, 2020.

[4] B. Gorti, G. Alexander, and R. Spee, "A novel, cost-effective stand-alone generator system," in *Proceedings of IEEE. AFRICON'96*, vol. 2, pp. 626–631, IEEE, 1996.

[5] A. Ferreira, R. Stephan, and M. Araujo, "Compensating characteristics of a brushless doubly-fed machine," in *2003 IEEE International Symposium on Industrial Electronics (Cat. No. 03TH8692)*, vol. 1, pp. 375–378, IEEE, 2003.

[6] Y. Liu, W. Ai, B. Chen, and K. Chen, "Control design of the brushless doubly-fed machines for stand-alone vscf ship shaft generator systems," *Journal of Power Electronics*, vol. 16, no. 1, pp. 259–267, 2016.

[7] P. Löhdefink, A. Dietz, and A. Möckel, "Direct drive concept for heavy-duty traction applications with the brushless doubly-fed induction machine," in *2018 Thirteenth International Conference on Ecological Vehicles and Renewable Energies (EVER)*, pp. 1–6, IEEE, 2018.

[8] P. Peng, X. Wang, A. Brugmann, L. Utt, E. Kline, J. Zhang, and L. Xu, "Design of a brushless doubly-fed machine for aviation turboelectric distributed propulsion," in *2020 IEEE Transportation Electrification Conference & Expo (ITEC)*, pp. 678–685, IEEE, 2020.

[9] S. Abdi, E. Abdi, A. Oraee, and A. McMahon, "Investigation of magnetic wedge effects in large-scale bdfms," 2013.

[10] J. Chen, X. Wang, T. Zhao, Z. Li, M. Kong, and P. Nie, "Application of brushless doubly-fed machine system in hydropower generation," in *2019 22nd international conference on electrical machines and systems (ICEMS)*, pp. 1–4, IEEE, 2019.

[11] P. Peng, L. Chen, X. Wang, R. Liu, A. Brugmann, L. Utt, E. Kline, J. Zhang, and L. Xu, "Design of a brushless doubly-fed machine for aviation electric propulsion," *IEEE Transactions on Industry Applications*, vol. 58, no. 5, pp. 6057–6068, 2022.

[12] S. Abdi, A. Grace, E. Abdi, and R. McMahon, "A new optimized rotor design for brushless doubly fed machines," in *2017 20th International Conference on Electrical Machines and Systems (ICEMS)*, pp. 1–6, IEEE, 2017.

[13] R. S. Rebeiro and A. M. Knight, "Characterization of a ducted rotor brushless doubly fed reluctance machine," *IEEE Transactions on Energy Conversion*, vol. 34, no. 1, pp. 79–87, 2018.

[14] S. Yu, Y. Zhang, C. Chen, F. Zhang, and H. Nian, "Loss estimation of brushless doubly-fed generator with hybrid rotor considering multiple influence factors," *IEEE Access*, vol. 8, pp. 60043–60051, 2020.

[15] S. Abdi, E. Abdi, A. Oraee, and R. McMahon, "Optimization of magnetic circuit for brushless doubly fed machines," *IEEE Transactions on Energy Conversion*, vol. 30, no. 4, pp. 1611–1620, 2015.

[16] S. Abdi, E. Abdi, H. Toshani, and R. McMahon, "Vibration analysis of brushless doubly fed machines in the presence of rotor eccentricity," *IEEE Transactions on Energy Conversion*, vol. 35, no. 3, pp. 1372–1380, 2020.

[17] O. Olubamiwa and N. Gule, "Design and optimization of a cage+ nested loops rotor bdfm," in *2020 International Conference on Electrical Machines (ICEM)*, vol. 1, pp. 1868–1874, IEEE, 2020.

[18] T. Staudt, F. Wurtz, N. J. Batistela, and P. Kuo-Peng, "Influence of rotor design and geometric parameter variation on global performance of brushless doubly-fed reluctance machines," in *2014 International Conference on Electrical Machines (ICEM)*, pp. 537–543, IEEE, 2014.

[19] S. Khaliq, S. Atiq, T. A. Lipo, and B.-I. Kwon, "Rotor pole optimization of novel axial-flux brushless doubly fed reluctance machine for torque enhancement," *IEEE Transactions on Magnetics*, vol. 52, no. 7, pp. 1–4, 2016.

[20] M. L. Adams, *Rotating machinery vibration: from analysis to troubleshooting*. CRC Press, 2009.

[21] A. Bisoi, A. Samantaray, and R. Bhattacharyya, "Sommerfeld effect in a gyroscopic overhung rotor-disk system," *Nonlinear Dynamics*, vol. 88, pp. 1565–1585, 2017.